HHS Public Access

Author manuscript

Ultrason Imaging. Author manuscript; available in PMC 2016 July 26.

Published in final edited form as:

Ultrason Imaging. 2016 January ; 38(1): 96–112. doi:10.1177/0161734615593747.

Multi-Wavelength Photoacoustic Visualization of High Intensity Focused Ultrasound Lesions

J. P. Gray[1], **N. Dana**[2], **K. L. Dextraze**[1], **F. Maier**[1], **S. Emelianov**[2], and **R. R. Bouchard**[1]

[1]MD Anderson Cancer Center, Houston, TX, USA

[2]University of Texas at Austin, Austin, TX, USA

Abstract

High intensity focused ultrasound (HIFU) thermal therapies are limited by deficiencies in existing image-guidance techniques. Previous studies using single-wavelength photoacoustic (PA) imaging have demonstrated that HIFU lesions generate contrast with respect to native tissues but have not sufficiently assessed lesion extent. The purpose of this study is to demonstrate feasibility of characterization of in vitro HIFU ablation lesion dimensions using 3D multi-wavelength PA imaging. Fresh porcine cardiac and liver tissue samples were embedded in agar phantoms and ablated using a 2.5 MHz small-animal HIFU system. Both 2D and 3D multi-wavelength photoacoustic-ultrasonic (PAUS) scans were performed in the near-infrared (NIR) range to characterize the change in the absorption spectrum of tissues following ablation and were compared to stained gross pathology to assess treatment margins and lesion extent. Comprehensive 2D multi-wavelength PA imaging yielded a spectrum in ablated tissue that did not display the characteristic local maximum in the optical absorption spectrum of deoxy-hemoglobin (Hb) near 760 nm. Two-dimensional tissue characterization map (TCM) images reconstructed from 3D TCM volumes reliably characterized lesion area and showed >70% area agreement with stained gross pathology. In addition, tissue samples were heated via water bath and concurrently interrogated with 2D PAUS imaging. PA signal exhibited an initial amplitude increase across all wavelengths, corresponding to an initial temperature increase, before then exhibiting a spectral change. This study suggests that multi-wavelength PA imaging has potential to obtain accurate characterization of HIFU lesion extent and may be better suited to guide HIFU ablation therapies during clinical treatments than single-wavelength methods.

Keywords

photoacoustic; HIFU; multi-wavelength; ablation; cardiac; liver; tissue characterization

Corresponding Author: R. R. Bouchard, MD Anderson Cancer Center, 1881 East Rd., Houston, TX 77054, USA. rrbouchard@mdanderson.org.

J. P. Gray and N. Dana contributed equally.

Declaration of Conflicting Interests

The author(s) declared no potential conflicts of interest with respect to the research, authorship, and/or publication of this article.

Introduction

High Intensity Focused Ultrasound

High intensity focused ultrasound (HIFU) is a minimally invasive technique that has developed significantly over the last two decades for the treatment of benign and malignant conditions in soft tissues.[1,2] HIFU treatments use ultrasound transducers with highly controlled beams to instantly achieve destructive temperatures at their focus. This technique has been used to treat targets that may be several centimeters below the skin surface, while preserving healthy tissue as hyperthermal therapy tends to occur at the focus of the beam.[2] HIFU is of clinical interest for several conditions, including atrial fibrillation of cardiac tissue,[3,4] central nervous system disorders of the brain,[5] treatment of both benign and malignant solid tumors through thermal ablation,[2] and enhanced drug delivery at treatment sites.[6] In the United States, HIFU has been indicated for clinical treatment of uterine fibroids and malignant bone metastases.[7]

Image guidance is employed during HIFU for treatment planning, tissue temperature, and assessment of tissue damage during and after treatment (i.e., estimating treatment margins).[2] Real-time image guidance has accommodated adaptive ablation planning, leading to increased efficacy of HIFU treatments and improved precision in estimating treatment margins.[2] Imaging guidance for hyperthermal therapy has been provided by magnetic resonance imaging (MRI), computed tomography (CT), and ultrasound (US), all of which have been able to elucidate anatomical structures and heating-probe location.[8] Several of these techniques have demonstrated the capability to monitor tissue temperature changes, yet only MRI is used as a standard-of-care technique for image guidance during clinical treatments.[9,10]

Photoacoustic Imaging

Photoacoustic (PA) imaging is a relatively novel technique that is gaining attention due to its feasibility of implementation as a point-of-care imaging solution, its molecular sensitivity, and its ready compatibility with existing US technology.[11] PA imaging can be achieved through extra-corporeal or interstitial application of near-infrared (NIR) laser pulses, which are absorbed by endogenous chromophores or exogenous contrast agents.[12,13] Due to the “optical window,” in which optical absorption by water, fat, and blood decreases dramatically in the NIR region (650–1100 nm), imaging depths of several centimeters can be achieved in soft tissues.[14] Photon energy absorbed by chromophores is converted into mechanical energy through a rapid thermal expansion, which results in the generation of an acoustic transient that propagates through soft tissue and may be detected by a standard US transducer at the tissue surface.[11,12] Detected signals can then be used to estimate a map of optical absorption with sub-millimeter spatial resolution. Because PA signals are detected using an ultrasonic transducer, PA images can be co-registered with US images.[11] These photoacoustic-ultrasonic (PAUS) images allow for the presentation of anatomical information alongside estimated optical absorption, and thus molecular composition, of the tissue.

The amplitude of PA pressure waves, p_0 ($\boldsymbol{r}, T, \lambda$), generated as a result of optical absorption by chromophores in tissue, are dependent on the speed of sound in tissue ($v_s(T)$ [cm s^{-1}]), a temperature-dependent volume expansion coefficient ($\beta(T)$ [K^{-1}]), the isobaric heat capacity in tissue ($C_p(T)$ [J kg^{-1} K^{-1}]), the optical absorption coefficient of the tissue ($\mu_{abs}(\boldsymbol{r}, \lambda)$ [cm^{-1}]), and the optical fluence ($\Phi(\boldsymbol{r}, \lambda)$ [J cm^{-2}]) as,[11–13]

$$p_0(r,T,\lambda)=\left(\frac{\beta(T)\,\nu_s^2(T)}{C_p(T)}\right)\mu_{abs}(r,\lambda)\Phi(r,\lambda). \quad (1)$$

Contrast in PA images arises from variations in the optical absorption coefficient, which depends on both the concentration of chromophores in tissue and the wavelength of the laser source. Due to the wavelength dependence of the optical absorption coefficient, multi-wavelength photoacoustic imaging can be performed by varying the wavelength of the laser through the entire NIR region to estimate the optical absorption properties of the tissue.[11,15] Varying the location of the PAUS transducer or using a 2D array and obtaining PA signals at several wavelengths allows for the generation of a multi-wavelength 3D PAUS volume. In addition, the temperature dependence of pressure wave generation may allow for real-time monitoring and characterization of temperature change during ablation.[16–19]

Current Image-Guidance Methods

Image-guidance techniques greatly improve the outcome of HIFU treatments by allowing physicians to more accurately and completely estimate treatment margins, yet existing imaging modalities are not entirely satisfactory for treatment guidance.[8,20,21] Currently, image guidance of HIFU treatments is performed using several standard imaging modalities. Traditional pulse-echo B-mode US provides excellent anatomical information and can provide short-term identification of hyperechoic regions of tissue corresponding to microbubble formation at the site of the HIFU focus; however, it cannot provide quantification of lesion extent.[22] Elastography can be used to assess and characterize induced lesions but can be difficult to implement in vivo and provide a significant number of false-positives.[23] Magnetic resonance imaging (MRI) allows for excellent identification of treatment targets, treatment planning, and real-time tracking of relative temperature changes at the site of ablation through MRI thermography,[9,10,24] but it is limited by the high cost and equipment incompatibility imposed by high magnetic field strengths. PA imaging is a promising modality for image guidance of HIFU therapies because of its ready compatibility with existing technology and capability to monitor target and healthy tissue during ablation with sub-millimeter spatial resolution. This level of spatial resolution in fact exceeds the spatial resolution of existing temperature MRI guidance techniques (1–2 mm).[2,25]

HIFU Guidance with PA Imaging

PA imaging provides several unique qualities that make it promising as an alternative to existing image-guidance techniques for HIFU. PA imaging is capable of both thermography and spectroscopy,[16,26,27] allowing for real-time assessment of temperature changes and tissue state. In practice, conventional US techniques such as Doppler imaging or

microbubble-contrast perfusion assessment can also be applied concurrently with PA imaging to assess nearby critical structures, such as vessels.[11]

Previous studies of HIFU ablations in vitro and in vivo using PA imaging have shown that PA imaging is capable of providing image contrast in the ablation region.[28–33] This change in contrast at the ablation site may be attributed to a change in the concentration of chromophores in the tissue as a result of heating.[34] However, single-wavelength methods typically fail to provide enough information to reliably quantify the precise position and dimensions of HIFU lesions. Studies using radio-frequency (RF) ablation have shown that multi-wavelength PA imaging is capable of detecting changes in the concentration of chromophores—specifically in the concentration of deoxy-hemoglobin (Hb)—following thermal ablation and that these multi-wavelength methods allow PA imaging to identify an optical absorption spectrum specific to ablated tissue and distinct from the typical Hb spectrum.[27,30] In this study, we use the previously described technique[27,30] in an in vitro environment following HIFU and water-bath ablation of cardiac and liver tissue samples. Both 2D and 3D multi-wavelength PA data of ablated tissue samples are then correlated to these two absorption spectra to create TCMs, which are used to quantitate lesion size for comparison with stained gross pathology. In addition, we examine the temperature dependence of the PA signal as tissue samples are heated in a phosphate buffered saline (PBS) bath.

Method

Sample Preparation and Ablation Procedure

Imaging samples were acquired from fresh porcine cardiac and liver tissues (Animal Technologies Inc., Tyler, Texas) within 24 hours of sacrifice and were never frozen. Excised tissues from one liver and two hearts were used to make three liver samples and three cardiac samples, each approximately $30 \times 30 \times 20$ mm^3 in size. Each specimen was embedded into an agar phantom for HIFU sonication. The HIFU transducer was acoustically coupled to the agar phantoms using ultrasound gel, and samples were each sonicated for 120 seconds at power settings between 22 and 30 watts using a LabFUS 2.5 MHz small-animal HIFU system (Image Guided Therapy Inc., Paris, France). Photographs of the HIFU system, HIFU transducer, and imaging system are presented in Figure 1. Following ablation, tissue specimens were removed from their agar phantoms, and the uppermost 1.5 to 2 mm of tissue surface was removed to expose ablation lesions to allow for tissue-sample photography and later co-registration with imaging data.

In addition, fresh bovine liver tissues (Animal Technologies Inc., Tyler, Texas) were acquired within 24 hours of sacrifice and never frozen. Two samples were excised from one liver and submerged in normal PBS in an imaging chamber containing a heat exchanger. The goal of this experiment was to monitor the tissue PA signal as a function of bath temperature. The tissue sample was located in the center of the copper tubing coil, which comprised the heat exchanger, to generate an approximately isotropic temperature field. Bath temperature was measured via thermocouple at a location a few millimeters from the upper surface of the tissue imaging plane.

Imaging Setup

Following the aforementioned ablation procedure, specimens were anchored in a thin layer of gelatin and submerged in normal PBS to achieve acoustic coupling between the tissue sample and the PAUS transducer. PAUS imaging was performed using a Vevo LAZR 2100 imaging system equipped with a 21 MHz US transducer coupled to a pulsed Nd:YAG laser capable of irradiating from 670 to 970 nm (FUJIFILM VisualSonics Inc., Toronto, Canada). In each sample, a single-wavelength 3D PAUS scan was performed over the extent of the tissue sample to identify a single plane containing the ablation lesion. The location of the lesion was chosen by selecting an area in the 3D PAUS scan exhibiting a hyperechoic US signal and high PA contrast. After identification of the lesion, a 2D comprehensive multi-wavelength PA scan was performed on this plane using wavelengths ranging from 680 to 970 nm in 3 nm steps. A multi-wavelength 3D PAUS scan was then performed on each tissue over a volume including the ablation lesion using five wavelengths in the NIR region (740, 750, 760, 780, 900 nm), corresponding to a distinct feature in the Hb absorption spectrum,[35] and averaging eight frames for each wavelength and location.

For the bath-heated samples, multi-wavelength PA imaging was done using five wavelengths in the NIR region (740, 750, 760, 770, 780 nm), corresponding to the same Hb spectral feature. First, a baseline multi-wavelength PA acquisition was performed. The bath-heat exchanger was then activated, and the tissue bath temperature rapidly rose to approximately 60°C. PA imaging at all wavelengths was conducted at 1-minute intervals for the first 30 minutes, then at 5-minute intervals thereafter, up to 60 minutes. Bath temperature was measured at each imaging time-point. Immediately post-imaging, the tissue sample was removed from the water bath and bisected at the imaging plane. Photographs were taken of the sample prior to heating, as well as at the point of bisection post-heating.

Staining Procedure

Following imaging, samples were stained using triphenyl tetrazolium chloride (TTC) salts for registration and comparison of gross pathology to PAUS data (Sigma-Aldrich Corp., St. Louis, Missouri). TTC is a redox indicator of metabolic activity: the white stain accumulates in cells and is oxidized to a deep red color by a variety of molecules associated with metabolic activity.[36,37] Tissue in the ablation region has undergone necrosis and should become white/gray in color, while metabolically active healthy tissue outside the ablation region will become a deep red. Staining solutions were prepared by dissolving 0.1 mg/mL TTC in normal PBS. Tissue samples were submerged in staining solution and incubated at 37°C for 20 minutes with constant stirring. After staining, tissue samples were patted dry and photographed. Bath-heated tissue samples were not stained as the tissue was clearly coagulated throughout the entire tissue volume.

2D Multi-Wavelength PA Analysis

The comprehensive 2D multi-wavelength scans were analyzed to assess whether HIFU treatment results in a change in the PA spectra of tissue. Regions of interest (ROI) were selected in areas showing high PA contrast and areas showing low PA contrast, corresponding to areas of ablated and non-ablated tissue, respectively. The mean PA signal inside each ROI was calculated for each wavelength scanned and plotted to display the

absorption spectra for ablated (liver and cardiac, respectively) and non-ablated tissue (Figure 2).

Creation of TCMs

TCMs were generated using a correlation-based algorithm. Reference absorption spectra for ablated and Hb absorbers were obtained from the comprehensive multi-wavelength PA data (liver or cardiac, as appropriate) using previously described methods.[27] The filtered PA data were compared to two reference spectra (i.e., Hb correlation and a distinct ablated correlation for each tissue type), resulting in two 3D datasets of Pearson correlation coefficients. These two 3D correlation datasets (i.e., Hb correlation coefficients and ablated correlation coefficients) were then processed with a simple thresholding algorithm. Correlation thresholds of 0.6 were used for both Hb and ablated reference spectra. PA voxels were then classified based on the respective thresholds and correlation coefficients. Voxels that correlated strongly (i.e., displayed correlation coefficients above the threshold) to only one reference spectra were classified accordingly (i.e., class 2 for ablated; class 1 for Hb). Voxels that correlated strongly to both were classified according to their greatest correlation coefficient. Voxels that correlated strongly to neither reference spectra were classified as 0 (no correlation). Thus, a trinary 3D TCM was constructed for each PA dataset and compared to photographed gross pathology. For the bath-treated tissue samples, an equivalent process was employed, save that a correlation threshold of 0.65 was used. A 2D TCM was generated at each time-point, and the 2D multi-wavelength PA signal was examined as a function of time (i.e., thermal exposure).

Image Registration and Characterization of Ablation Size

HIFU 3D TCM data were co-registered with top-view photographs of stained gross pathology by manual registration based on corresponding visual landmarks. Top-view C-scan TCMs were obtained by taking the mode along the depth axis for each voxel at the surface of the TCM volume. Mode calculations were performed from a depth 0.184 mm (corresponding to 5 voxels, which tended to avoid subsurface fluence artifacts) below the surface of the volume to a depth 1.29 mm (corresponding to 35 voxels) below the surface. Borders between areas of ablation and non-ablation were manually segmented in matched TCMs and pathology photographs by three experts, generating three segmentations for each TCM or pathology photograph. The segmentations for each TCM or photograph were analyzed automatically using MATLAB. Pixel-wise lesion area was calculated from each expert-segmentation of corresponding TCM data and gross pathology photographs. The mean and standard deviation of lesion areas from the expert segmentations were calculated and subsequently converted to physical dimensions (mm^2). Percent area agreement between gross pathology and TCMs was calculated for each tissue sample as,

$$\%\text{Area Agreement}=1-\frac{|\text{Segmented Image Area}-\text{Segmented Pathology Area}|}{\text{Segmented Pathology Area}}. \quad (2)$$

An SNR analysis was done, comparing SNR up to 8 mm tissue depth, while varying the number of averages. A 0.21 × 0.18 mm^2 sliding kernel was used, analyzing signal along a depth line located in the center of the ROI shown in Figure 5(A). In addition, a noise image was acquired (degassed water, no laser irradiation) to assess PA image noise at the equivalent depth. Up to 64 averages were used. Analysis was done on beam-formed image data, using the following equation:

$$\mathbf{SNR}=10\cdot\mathbf{log}_{10}\left(\frac{\overline{\boldsymbol{PA}}}{\sigma_{\mathrm{noise}}}\right), \quad (3)$$

where $\overline{PA}$ and σ_{noise} denote the ROI mean PA signal and noise standard deviation, respectively. The SNR threshold was empirically determined by analyzing the depth, and thus corresponding SNR, at which the TCM loses continuity (i.e., the point at which the gaps/inconsistencies in the solid TCM regions become as large as or greater than the spatial averaging kernel used).

Results

2D Multi-Wavelength PA Analysis

Figure 2 displays the results of 2D multi-wavelength PA imaging performed in liver tissue. Figure 2(A) shows an overlay of the single-wavelength PA signal at 710 nm on its matched US image. ROIs shown in Figure 2(A) represent the area averaged at each wavelength to generate the reference spectra from ablated and non-ablated tissue; these spectra are shown in Figure 2(B). We expect the dominant absorber to be Hb in this wavelength region as the ex vivo tissue samples should be oxygen-depleted.[14] Non-ablated tissue displays an absorption spectrum that agrees well with that of Hb[27] as the characteristic local maximum in the absorption spectrum around 760 nm is readily apparent. The absorption spectrum in the ROI corresponding to ablated tissue decreases monotonically with increasing optical wavelength and does not display the characteristic 760 nm local maximum of the Hb absorption spectrum, indicating a likely change in the concentration of Hb absorbers due to hyperthermia.

Lesion Area Statistics

TCMs were created by correlating to wavelengths in the region between 740 and 780 nm; the region where ablated tissue and Hb absorption spectra are most distinct. Tissue characterization was achieved at depths up to 3 mm below the surface of the tissue, while gross pathology indicated that lesions extend 5 to 7 mm in depth. Examples of 3D TCM volumes overlaid on matching US volumes for liver and cardiac tissues are shown in Figure 3.

Results of area calculations performed on manually segmented lesions in both TCMs and gross pathology photographs can be found in Table 1; a representative sample image can be found in Figure 4. In TCM volumes, we observed areas of tissue bordering the areas of strong ablation correlation that correlated poorly to both ablated and non-ablated absorption

spectra. These areas were segmented in addition to the area that was primarily classified as the lesion and was also compared to gross pathology.

For the bath-heated samples, Figures 5(A) to (E) show a 2D TCM overlaid on co-registered B-mode US images for 5 time-points, with a rectangular square identifying an ROI for spectral analysis. At baseline (Figure 5A), strong correlation to Hb is observed to approximately 4 mm in depth across the entire width of the tissue sample. The depth of this correlation decreases to about 2 mm by 15 minutes (Figure 5B). By 30 minutes, a thin layer correlating to ablated tissue can be identified at the tissue surface (Figure 5C). At 45 minutes, 1 to 2 mm of ablated tissue is identified at the surface, with only sporadic Hb identified beneath the surface, and this trend continues at 60 minutes (Figure 5E). Figure 5(F) shows a surface plot of the mean PA signal of the ROI, normalized to baseline, as a function of wavelength and time. The PA signal rapidly increases for the first 5 minutes after heating onset, but still maintains the Hb spectral shape (local maximum at 760 nm). Amplitude decreases slightly, but spectral shape is maintained until approximately 30 minutes, at which point the spectra begin to flatten, correlating more strongly to the ablated reference spectra thereafter (as shown by the surface color). Figure 5(G) allows for better comparison of the spectra at prominent time-points. Note that at 5 minutes after heating onset (bath temperature of 52°C), a PA signal increase of approximately 80% from baseline can be seen across all wavelengths. The signal decreases slightly, but remains relatively constant at roughly 50% above baseline until about 30 minutes after heating onset. At 30 minutes, we can see the PA spectrum flattening out, and by 45 and 60 minutes, we observe a monotonically decreasing spectrum that strongly resembles the ablated reference spectrum for liver.

Analysis of TCMs against the SNR results suggests that an SNR of 10 dB is generally sufficient for reliable tissue characterization using this method. By increasing averages, we found SNR using this method can be improved approximately proportional to $\sqrt{\#averages}$, allowing accurate TCMs at greater depths in tissue, although at the cost of increased imaging time.

Discussion

In this initial study, we demonstrate that multi-wavelength PA imaging can provide estimates of lesion extent with gross pathology area agreement greater than 79% in liver and greater than 70% in cardiac tissue. As has been shown previously[29,32,33] and demonstrated in this study (Figure 2), high PA-signal contrast in the ablated lesion center can be obtained using a single laser wavelength. However, PA imaging data from a single wavelength tend not to be sufficient to completely characterize the extent of the ablation lesion. Although single-wavelength PA imaging may be useful to perform a quick 3D scan and obtain a rough identification of the lesion center, multi-wavelength TCMs provide significantly more information about the boundaries and extent of ablation lesions, as shown by comparing Figures 2(A), 3(B), and 5(A) to (E). Focusing on the wavelengths where the absorption spectra of ablated and non-ablated tissue display different features, multi-wavelength TCMs were able to identify HIFU ablation lesions in ex vivo cardiac and liver tissue and obtain area agreement with gross pathology photographs in excess of 70% and with sub-millimeter

spatial resolution. TCMs compared well with manually segmented gross pathology photographs (minimum 70% area agreement), demonstrating multi-wavelength PA imaging as a potential tool for HIFU lesion identification and quantification.

Despite our success in the identification and characterization of HIFU ablation lesions in cardiac and liver tissues, limitations in PA imaging and our experimental setup prevent ideal characterization of lesion dimensions. Imaging artifacts immediately at the surface of the tissue were observed and are believed to be the result of subsurface photon fluence and refractive index discontinuities between the surface of the tissue and the PBS used to couple the tissue to the ultrasound transducer. In our study, these artifacts were mitigated when creating 2D TCM images of the top-view plane by using a depth 0.184 mm below the tissue surface as the starting point for reconstruction of the C-scan projected views.

PA-based TCMs also underestimated lesion depth in this experiment. Depth of PA imaging is limited by scattering of photons, which increases the likelihood of absorption by chromophores at shallower depths in the tissue. In this experiment, imaging depths were limited to no more than 3 mm below the surface of the tissue, yet HIFU lesions extended 5 to 7 mm in depth. Several techniques could be employed to increase the penetration depth of imaging, including increased photon fluence and increased frame averaging to improve the signal-to-noise ratio at depth, as discussed below. Interstitial delivery of light by laser fibers also allows for significantly deeper light delivery to provide image guidance of treatments on deep-lying tissues, such as the liver and kidneys.[38] By employing these methods, it should be possible to extend imaging depth beyond 3 mm. In addition, penetration depth could possibly be improved in in vivo experiments due to the fact that tissues will be highly oxygenated. Optical absorption by oxygenated hemoglobin is roughly an order of magnitude lower in the NIR spectrum than that of Hb.[15] This reduction in optical absorption may allow increased optical penetration depth while maintaining energy, but it may require re-optimizing imaging wavelengths to maintain contrast between ablated and native oxygenated tissue.

A noteworthy effect observed in this experiment was the appearance of a ring of tissue surrounding the area correlating to ablated tissue in TCMs that did not correlate well to either the obtained ablated tissue spectrum or the standard Hb spectrum. This effect was observed in both liver and cardiac tissue in our study and has been reported in previous studies.[27] In cardiac tissues, the area of non-correlation was not always observed. An example of this effect is seen in Figure 4(C), where an area of non-correlated tissue (i.e., black) borders the upper area correlating highly to ablated tissue (i.e., red) at the core of the lesion. The segmentation region containing the region of ablation-correlated (red) and non-correlated (e.g., also including the black region extending from 4 to 6 mm in elevation in Figure 4C) tissue showed better agreement with segmented ablation regions in gross pathology photographs than the segmentations of the ablation-correlated region alone. Regions of ablation correlation alone tended to underestimate the area extent of lesions when compared to gross pathology segmentations. The change in the PA spectrum in ablated tissue likely results from hyperthermia-induced changes in the Hb chromophore. It is possible that incomplete conversion of Hb occurs at the edge of the ablation region due to

reduced increase in local temperature as compared to the core of the lesion, resulting in an absorption spectrum that did not correlate well to either Hb or the lesion core.

The capacity of PA imaging to assess temperature has been previously demonstrated by examining changes in PA amplitude.[16,19] By applying similar techniques, we were able to track the relative temperature rise in the bath-heated tissue sample during the first several minutes. As shown in Figure 5(F), the PA amplitude then decreases slightly after five minutes. We suspect this is primarily a result of changes in surface fluence. As can be seen in the B-mode US images in Figure 5, the tissue swells initially (B and C), before contracting partially (D and E). This initial tissue swelling is likely the result of increased osmotic pressure in the bath, following temperature increase. The swelling is likely to affect the surface fluence, due to a change in separation between the tissue and light emission source. The tissue contraction observed in Figures 5(D) and (E) is likely due to the coagulation of extra-cellular matrix (ECM) proteins, which concurs with the observed strong correlation of the PA signal to the ablated reference spectrum (red region in figures). These results highlight the potential complementary nature of PA thermography and multi-wavelength analysis. Tissue coagulation may also explain the decrease in PA amplitude after 30 minutes, as increased optical scattering following coagulation will reduce fluence, and thus PA signal, at greater depths. While these factors confound PA thermography in this experiment, these issues may not be as prevalent in clinical applications for several reasons. First, tissue hyperthermal therapy typically occurs on the order of several seconds to a few minutes and is typically much more spatially localized, which may reduce large scale tissue swelling or edema. Last, if an optical scattering increase within an ROI correlates to a change in the observed PA spectra, as suggested by this study, it may serve as a partial endpoint for hyperthermal therapy, rather than a mitigating factor to image guidance. Furthermore, if changes in optical fluence and absorption can be accounted for (perhaps by collecting some backscattered light for diffuse reflectance assessment[39]), PA thermography may be able to quantify thermal dose, comparable to what is currently done using MRI thermography.

The SNR analysis suggests that roughly 10 dB SNR is necessary for reliable TCM analysis. Our particular system showed that, with 64 averages, the SNR up to 5 mm can be improved to allow for reliable TCM analysis. Although increased averaging may be prohibitive in some clinical applications, such as cardiac imaging, this analysis suggests a baseline to predict TCM accuracy as a function of depth for a given application and imaging system.

Future Work

Development of in vivo imaging solutions will be necessary to apply PA imaging clinically for guidance of HIFU treatments. Although development of an in vivo system for combined HIFU therapy and PAUS imaging will not be a trivial task, building upon previous work by Cui et al.[29,31,32] and Prost et al.[40] may improve single-device integration, which allows straightforward co-registration of HIFU ablation space with PA and US imaging spaces. This would overcome a significant hurdle for clinical translation.

Real-time image guidance remains a currently unrealized goal for developing PA imaging systems. While this study used a laser source with a pulse repetition frequency (20 Hz) that

limited acquisition to near-real-time imaging (five single-wavelength frames per second, without averaging), commercial laser systems operating at kilohertz pulse repetition frequencies are readily available at select wavelengths, albeit sometimes with lower pulse energies. These systems may allow PA imaging, with proper wavelength selection, to achieve complete real-time image guidance exceeding 30 frames per second.[27]

Corroboration of these results in an in vivo model is necessary to confirm that the findings reported here are relevant to further clinical application. One recent study[28] has reported inconclusive findings, showing that while most single-wavelength ex vivo studies reported positive PA contrast in the ablation lesion, it is possible to observe negative contrast in ablation lesions in vivo. One proposed explanation is that variations in thermal deposition between in vivo and ex vivo models may lead to a different distribution of chromophores between the two environments. As our method relies upon correlation to multiple laser wavelengths, it may be possible to identify a difference in the chromophores present in the ablated regions of in vivo and ex vivo models. Although the data in this study suggest Hb is present in significant quantities before ablation and is significantly reduced following ablation, it is not clear which chromophore(s) is generating PA signal in the ablated region. Previous work has suggested that increased temperatures during thermal therapy may give rise to a variety of hemoglobin derivatives, which may account for the observed contrast between normal and ablated tissue.[34,41,42] Although production of hemoglobin derivatives is often cited as a potential source of contrast in ablated tissues, to our knowledge, no study has shown definitively that the proposed derivatives are produced in significant concentrations in tissue. Studies of the thermal unfolding and aggregation process of hemoglobin using 2D infrared spectroscopy have shown that thermal degradation is a complex, multi-step process that is irreversible once local tissues reach a certain temperature threshold: initial destabilizations in the structure of hemoglobin occur at low temperatures between 30°C to 44°C. complete thermal unfolding occurs between 44°C to 54°C. and irreversible aggregation of the denatured protein occurs at temperatures above 54°C.[43] This complex, three-stage denaturation process involves several potentially irreversible conformation changes in the structure of hemoglobin. Given the dependence of protein optical absorption on the 3D structure of the protein, these irreversible, temperature-dependent structural changes in hemoglobin may explain the observed elimination of the 760 nm peak in the Hb spectrum in ablated tissue. Partial unfolding of Hb may yield a range of different absorption spectra in ablated tissues rather than a single absorption spectrum corresponding to a single chromophore. This range of unfolding states could explain the observed correlation discrepancies at the edges of tissue lesions and could be developed to benchmark levels of partial tissue coagulation. In future studies, it would be useful to submit samples of ablated and non-ablated tissues to hemopathological and chemical assays to identify with confidence which chromophores are present and in what concentration before and after ablation.

PA-based temperature monitoring must also account for changes in optical absorption and fluence. A previous study[44] monitored the PA-signal ratio at two different wavelengths during tissue heating, verifying that PA-signal variations occur consistently across wavelengths until the tissue undergoes a change of state (i.e., thermal coagulation), as we observed. By analyzing complementary PA-signal amplitude and multi-wavelength techniques used herein with more applicable hyperthermia models (RF- and HIFU-

hyperthermal therapy using in vivo models), we can better evaluate and improve their utility, which is paramount to implementing real-time imaging guidance for thermal treatment.

Conclusion

We have demonstrated the feasibility of using multi-wavelength PA imaging to create tissue characterization volumes that allow the differentiation of HIFU-induced tissue ablation lesions from non-ablated tissue and to estimate the treatment margins of tissue ablations in 2D planes in ex vivo cardiac and liver tissue samples following a HIFU ablation. Multi-wavelength PA imaging demonstrates that HIFU-induced hyperthermia results in changes in the Hb absorption spectrum that can be leveraged for PA-based segmentation. Multi-wavelength TCMs were used to successfully identify lesion size with a greater accuracy than single-wavelength methods. Multi-wavelength TCMs agreed with gold-standard stained pathology images (70% area agreement) and were able to successfully assess lesion margins with a spatial resolution comparable to existing temperature MRI techniques. In addition, we demonstrated the complementary nature of PA thermography and multi-wavelength TCMs. Furthermore, in vivo experiments concurrent with treatment must be performed to assess PA-signal changes in living tissues. These results suggest that multi-wavelength PA imaging and PA thermography present a promising modality for guiding hyperthermia therapies that depend on precise knowledge of temperature and lesion extent to preserve critical structures.

Acknowledgments

The authors would like to thank Dr. Jason Stafford, Oguzhan Ege, Charles Kingsley, Trevor Mitcham, and Houra Marta Taghavi for assisting with experiments. We would also like to thank Jordan Roos for administrative assistance.

Funding

The author(s) disclosed receipt of the following financial support for the research, authorship, and/or publication of this article: This work was funded, in part, by a Cancer Prevention and Research Institute of Texas Julia Jones Mathews Scholarship, an NIH Shared Instrumentation Grant (S10 OD010403), and an NIH Cancer Center Support Grant (P30 CA016672).

References

1. Bailey MR, Khokhlova VA, Sapozhnikov OA, Kargl SG, Crum LA. Physical mechanisms of the therapeutic effect of ultrasound (a review). Acoust Phys. 2003; 49(4):369–88.
2. Kennedy JE. High-intensity focused ultrasound in the treatment of solid tumours. Nat Rev Cancer. 2005; 5:321–7. [PubMed: 15776004]
3. Lee LA, Simon C, Ph D, Bove EL, Mosca RS, Ebbini ES, et al. High intensity focused ultrasound effect on cardiac tissues: potential for clinical application. Echocardiography. 2000; 17(6):563–6. [PubMed: 11000591]
4. Groh M, Binns O, Burton H, Ely S, Johnson A. Ultrasonic cardiac ablation for atrial fibrillation during concomitant cardiac surgery: long-term clinical outcomes. Ann Thorac Surg. 2007; 84(6): 1978–83. [PubMed: 18036920]
5. Jagannathan J, Sanghvi NT, Crum LA, Yen CP, Medel R, Dumont AS, et al. High-intensity focused ultrasound surgery of the brain: part 1-A historical perspective with modern applications. Neurosurgery. 2009; 64(2):201–10. [PubMed: 19190451]
6. Dromi S, Frenkel V, Luk A, Traughber B, Angstadt M, Bur M, et al. Pulsed-high intensity focused ultrasound and low temperature-sensitive liposomes for enhanced targeted drug delivery and antitumor effect. Clin Cancer Res. 2007; 13(9):2722–7. [PubMed: 17473205]

7. U.S. Food and Drug Administration Center for Devices and Radiological Health. InSightec ExAblate® System, Model 2000/2100/2100 VI approval letter. 2012. Available from: http://www.accessdata.fda.gov/cdrh_docs/pdf11/p110039a.pdf
8. Goldberg SN, Grassi CJ, Cardella JF, Charboneau JW, Dodd GD, Dupuy DE, et al. Image-guided tumor ablation: standardization of terminology and reporting criteria. J Vasc Interv Radiol. 2005; 16(6):765–78. [PubMed: 15947040]
9. Hynynen, K.; Damianou, C.; Darkazanli, A.; Unger, E.; Levy, M.; Schenck, JF. On-line MRI monitored non-invasive ultrasound surgery. 14th Annu Int Conf IEEE Eng Med Biol Soc; 1992; p. 350-1.
10. Jolesz F. MRI-guided focused ultrasound surgery. Annu Rev Med. 2009; 60:417–30. [PubMed: 19630579]
11. Bouchard RR, Sahin O, Emelianov SS. Ultrasound-guided photoacoustic imaging: current state and future development. IEEE Trans Ultrason Ferroelectr Freq Control. 2014; 61(3):450–66. [PubMed: 24569250]
12. Xu M, Wang LV. Photoacoustic imaging in biomedicine. Rev Sci Instrum. 2006; 77(4):041101.
13. Beard P. Biomedical photoacoustic imaging. Interface Focus. 2011; 1(4):602–631. [PubMed: 22866233]
14. Smith AM, Mancini MC, Nie S. Bioimaging: second window for in vivo imaging. Nat Nanotechnol. 2009; 4(11):710–1. [PubMed: 19898521]
15. Mallidi S, Luke GP, Emelianov S. Photoacoustic imaging in cancer detection, diagnosis, and treatment guidance. Trends Biotechnol. 2011; 29(5):213–21. [PubMed: 21324541]
16. Shah J, Park S, Aglyamov S, Larson T, Ma L, Sokolov K, et al. Photoacoustic imaging and temperature measurement for photothermal cancer therapy. J Biomed Opt. 2008; 13(3):034024. [PubMed: 18601569]
17. Larin KV. Monitoring of temperature distribution in tissues with optoacoustic technique in real time. Proc SPIE. 2000; 3916:311–21.
18. Larina IV, Larin KV, Esenaliev RO. Real-time optoacoustic monitoring of temperature in tissues. J Phys D: Appl Phys. 2005:2633–9.
19. Pramanik M, Wang LV. Thermoacoustic and photoacoustic sensing of temperature. J Biomed Opt. 2009; 14(5):054024. [PubMed: 19895126]
20. Schlesinger D, Benedict S, Diederich C, Gedroyc W, Klibanov A, Larner J. MR-guided focused ultrasound surgery, present and future. Med Phys. 2013; 40(8):080901. [PubMed: 23927296]
21. Rosenthal EL, Warram JM, Bland KI, Zinn KR. The status of contemporary image-guided modalities in oncologic surgery. Ann Surg. 2015; 261(1):46–55. [PubMed: 25599326]
22. Vaezy S, Shi X, Martin RW, Chi E, Nelson PI, Bailey MR, et al. Real-time visualization of high-intensity focused ultrasound treatment using ultrasound imaging. Ultrasound Med Biol. 2001; 27(1):33–42. [PubMed: 11295268]
23. Righetti R, Kallel F, Stafford RJ, Price RE, Krouskop TA, Hazle JD, et al. Elastographic characterization of HIFU-induced lesions in canine livers. Ultrasound Med Biol. 1999; 25:1099–1113. [PubMed: 10574342]
24. Ottenhausen M, Bodhinayake I, Banu M, Kesavabhotla K, Ray A, Boockvar JA. Industry progress report on neuro-oncology: biotech update 2013. J Neurooncol. 2013; 115(2):311–6. [PubMed: 23949146]
25. Quesson B, de Zwart J, Moonen C. Magnetic resonance temperature imaging for guidance of thermotherapy. J Magn Reson Imaging. 2000; 12(4):525–33. [PubMed: 11042633]
26. Lee HJ, Liu Y, Zhao J, Zhou M, Bouchard RR, Mitcham T, et al. In vitro and in vivo mapping of drug release after laser ablation thermal therapy with doxorubicin-loaded hollow gold nanoshells using fluorescence and photoacoustic imaging. J Control Release Soc. 2013; 172(1):152–8.
27. Dana N, Di Biase L, Natale A, Emelianov S, Bouchard R. In vitro photoacoustic visualization of myocardial ablation lesions. Heart Rhythm. 2014; 11(1):150–7. [PubMed: 24080065]
28. Chitnis PV, Brecht H-P, Su R, Oraevsky AA. Feasibility of optoacoustic visualization of high-intensity focused ultrasound-induced thermal lesions in live tissue. J Biomed Opt. 2010; 15(April): 021313. [PubMed: 20459235]

29. Cui H, Staley J, Yang X. Integration of photoacoustic imaging and high-intensity focused ultrasound. J Biomed Opt. 2010; 15(2):021312. [PubMed: 20459234]
30. Sun Y, O'Neill B. Imaging high-intensity focused ultrasound-induced tissue denaturation by multi-spectral photoacoustic method: an ex vivo study. Appl Opt. 2013; 52:1764–70. [PubMed: 23478783]
31. Cui H, Yang X. In vivo imaging and treatment of solid tumor using integrated photoacoustic imaging and high intensity focused ultrasound system. Med Phys. 2010; 37:4777–81. [PubMed: 20964197]
32. Cui H, Yang X. Real-time monitoring of high-intensity focused ultrasound ablations with photoacoustic technique: an in vitro study. Med Phys. 2011; 38(10):5345–50. [PubMed: 21992353]
33. Funke AR, Aubry JF, Fink M, Boccara AC, Bossy E. Photoacoustic guidance of high intensity focused ultrasound with selective optical contrasts and time-reversal. Appl Phys Lett. 2009; 94:054102.
34. Khokhlova TD, Pelivanov IM, Sapozhnikov OA, Solomatin VS, Karabutov AA. Opto-acoustic diagnostics of the thermal action of high-intensity focused ultrasound on biological tissues: the possibility of its applications and model experiments. Quantum Electron. 2006; 36(12):1097–1102.
35. Kim JG, Xia M, Liu H. Extinction coefficients of hemoglobin for near-infrared spectroscopy of tissue. IEEE Eng Med Biol Mag. 2005; 24:118–21. [PubMed: 15825855]
36. Black M, Kleiner I. The use of triphenyltetrazolium chloride for the study of respiration of tissue slices. Science. 1949; 110(2868):660–1. [PubMed: 15396020]
37. Berridge MV, Tan ANS, Mccoy KD, Wang RUI. The biochemical and cellular basis of cell proliferation assays that use tetrazolium salts. Biochemica. 1996; 4:4–9.
38. Mitcham, T.; Marques, T.; Chatterjee, D.; Krishnan, S.; Pugh, T.; Bouchard, R. Transrectal photoacoustic-ultrasonic imaging enhancement through interstitial irradiation and targeted nanoparticles. Proceedings of the 2013 IEEE Ultrasonics Symposium; Prague, Czech Republic. July, 2013;
39. Hennessy R, Lim SL, Markey MK, Tunnell JW. Monte Carlo lookup table-based inverse model for extracting optical properties from tissue-simulating phantoms using diffuse reflectance spectroscopy. J Biomed Opt. 2013; 18(3):037003. [PubMed: 23455965]
40. Prost A, Funke A, Tanter M, Aubry J-F, Bossy E. Photoacoustic-guided ultrasound therapy with a dual-mode ultrasound array. J Biomed Opt. 2012; 17:061205. [PubMed: 22734735]
41. Farahani K, Saxton RE, Yoon HC, De Salles AAF, Black KL, Lufkin RB. MRI of thermally denatured blood: methemoglobin formation and relaxation effects. Magn Reson Imaging. 1999; 17:1489–94. [PubMed: 10609997]
42. Black JF, Barton JK. Chemical and structural changes in blood undergoing laser photocoagulation. Photochem Photobiol. 2004; 80:89–97. [PubMed: 15339203]
43. Yan Y-B, Wang Q, He H-W, Zhou H-M. Protein thermal aggregation involves distinct regions: sequential events in the heat-induced unfolding and aggregation of hemoglobin. Biophys J. 2004; 86:1682–90. [PubMed: 14990496]
44. Hsiao Y-S, Wang X, Deng CX. Dual-wavelength photoacoustic technique for monitoring tissue status during thermal treatments. J Biomed Opt. 2013 18.067003.

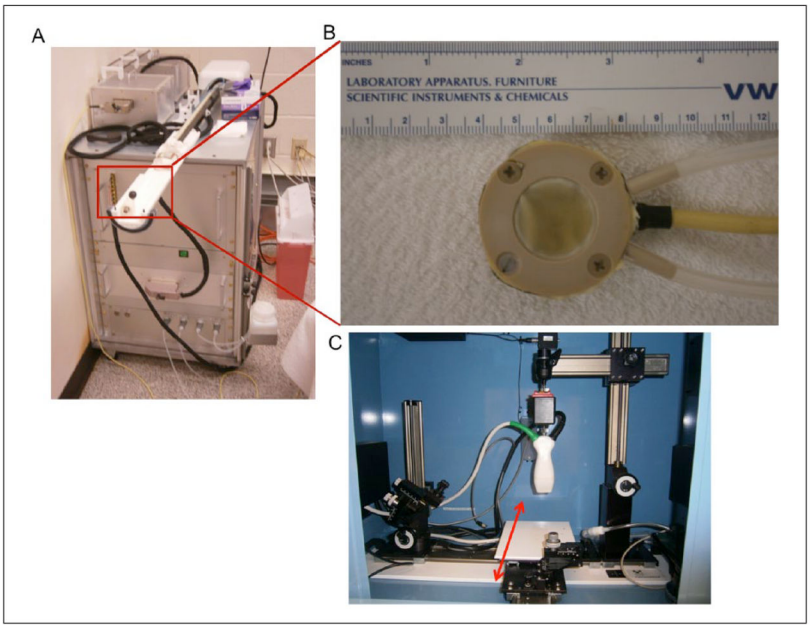

Figure 1.

Photographs of experimental equipment: (A) LabFUS 2.5 MHz small-animal HIFU system; (B) close-up view of eight-element, 2.5 MHz HIFU transducer; and (C) Vevo LAZR 2100 combined PAUS imaging system. Red arrow indicates motorized platform for elevation scanning during 3D imaging. HIFU = high intensity focused ultrasound; PAUS = photoacoustic ultrasonic.

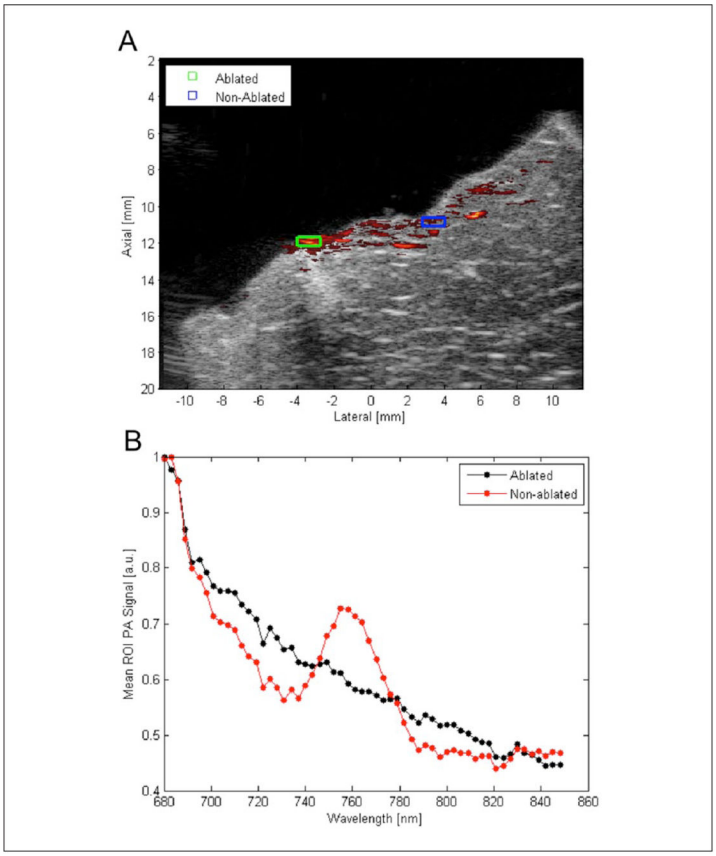

Figure 2.

Results of 2D comprehensive multi-wavelength PA imaging: (A) overlay of single-wavelength PA data at 710 nm on matched US image. High PA contrast and US hyperechogenicity exhibited in area where lesion is expected; (B) plot of mean PA signal in each ROI indicated at each wavelength. Mean PA spectrum in areas outside lesion exhibit the characteristic peak of Hb around 760 nm; peak not seen in area of high PA contrast where lesion is expected. PA = photoacoustic; US = ultrasound; ROI = regions of interest; Hb = deoxy-hemoglobin.

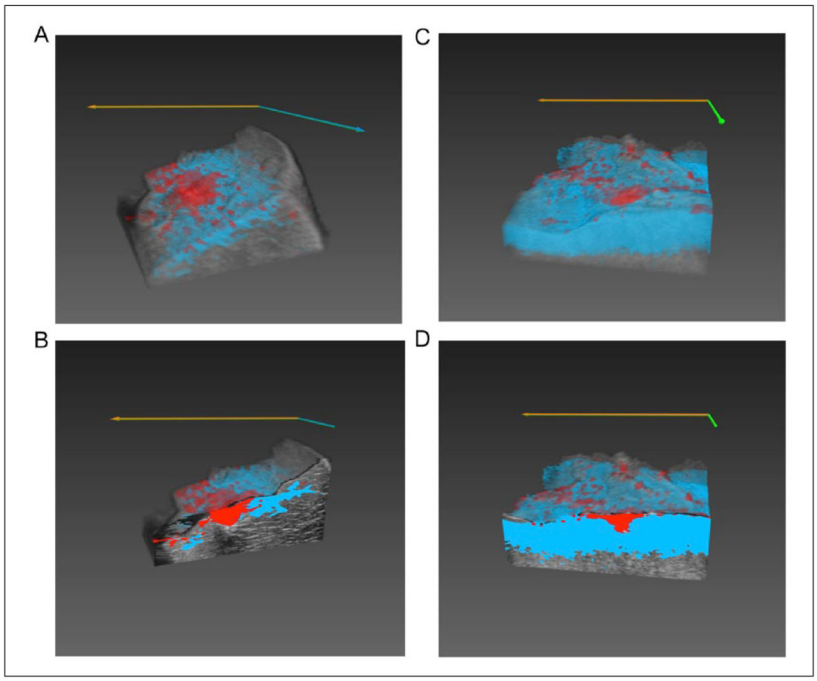

Figure 3.

Renderings of 3D TCM volumes overlaid matching 3D US volumes: (A) full liver sample 3D volume rendering; and (B) cut-away view of 2D frame in the interior of the lesion of the same liver volume; (C) full cardiac sample 3D volume rendering; and (D) cut-away view of 2D frame in the interior of the lesion of same cardiac volume. TCM = tissue characterization map; US = ultrasound.

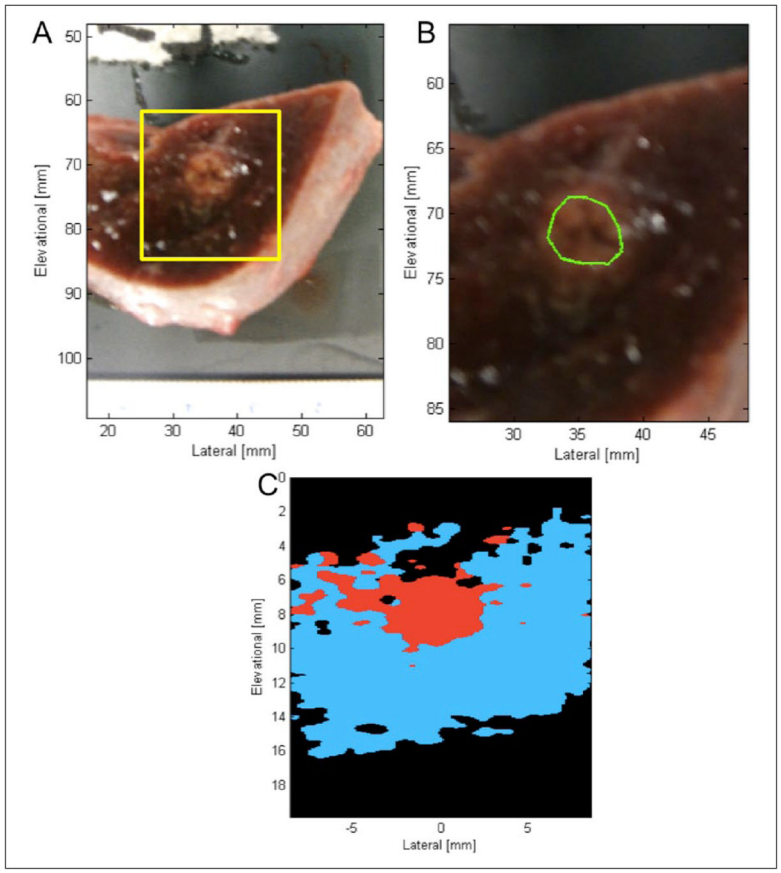

Figure 4.

Comparison of gross pathology and TCM data for one liver tissue sample: (A) photographed stained gross pathology. Yellow box indicates area of tissue displayed by 2D TCM data; (B) zoomed in photograph of stained gross pathology. Manual segmentation of gross pathology overlaid in green; (C) C-scan 2D TCM plane reconstructed from TCM volume for manual segmentation. Blue indicates Hb correlation, red indicates ablated spectrum correlation, black indicates correlation to neither spectra. TCM = tissue characterization map.

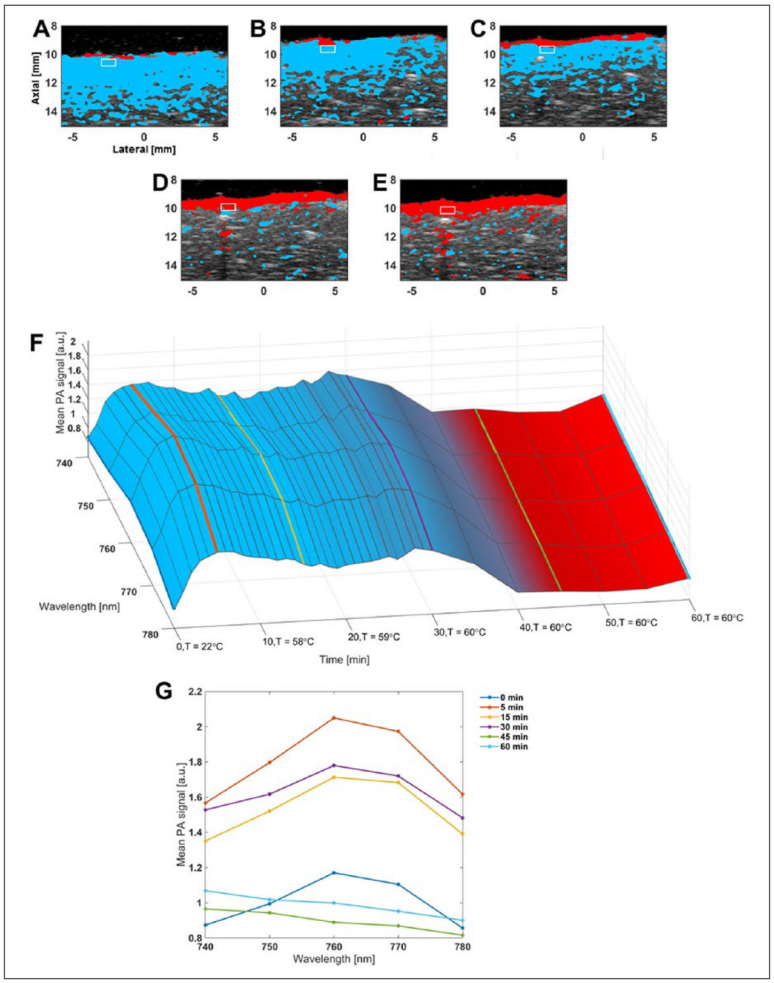

Figure 5.

Comparison of TCMs (same color-coding as previously stated) and spectra for sample subjected to PBS-bath thermal treatment: (A) to (E) TCMs overlaid on co-registered US B-mode image for time-points 0 (baseline), 15, 30, 45, and 60 minutes of thermal treatment, respectively. White rectangular box denotes a 1 × 0.5 mm^2 ROI selected for analysis, maintained at constant depth from tissue surface; (F) surface plot of mean PA signal in ROI (normalized to baseline), as a function of wavelength and time. Surface color-map represents mean TCM color value across ROI at each time-point; (G) PA-signal spectra from F for time-points 0, 5, 15, 30, 45, and 60 minutes (time-points at 0, 15, 30, 45, and 60 minutes correspond to images A to E, respectively). TCM = tissue characterization map; PBS = phosphate buffered saline; US = ultrasound; PA = photoacoustic; ROI = regions of interest.

Table 1

Results of area calculations performed on manually segmented lesions in both TCMs and gross pathology photographs.

	Liver 1	Liver 2	Liver 3	Cardiac 1	Cardiac 2	Cardiac 3
Pathology area (mm^2)	16.9 ± 1.8	35.3 ± 3.7	22.2 ± 2.0	11.4 ± 1.0	10.3 ± 0.1	3.5 ± 0.2
Combined ablated core and non-correlation region area (mm^2)	15.7 ± 1.9	28.1 ± 0.2	22.2 ± 0.1	11.5 ± 0.4	7.21 ± 0.2	3.2 ± 0.1
% Area agreement combined ablated core and non-correlation region	93.2%	79.8%	99.9%	99.1%	70.0%	91.7%
Ablated core area	8.53 ± 0.1	25.6 ± 0.1	20.0 ± 0.1	11.6 ± 0.6	7.2 ± 0.2	2.1 ± 0.2
% Area agreement ablated core	50.6%	72.5%	90.2%	98.3%	70.1%	61.2%